The Journal of Chemical Physics

High-resolution sub-Doppler infrared spectroscopy of atmospherically relevant Criegee precursor CH_2I radicals: CH_2 stretch vibrations and "charge-sloshing" dynamics

Cite as: J. Chem. Phys. **148**, 174308 (2018); https://doi.org/10.1063/1.5028287
Submitted: 08 March 2018 . Accepted: 16 April 2018 . Published Online: 04 May 2018

A. Kortyna, D. M. B. Lesko, and D. J. Nesbitt

High-resolution sub-Doppler infrared spectroscopy of atmospherically relevant Criegee precursor CH_2I radicals: CH_2 stretch vibrations and "charge-sloshing" dynamics

A. Kortyna,[1] D. M. B. Lesko,[2] and D. J. Nesbitt[1,2,3]
[1]*JILA, National Institute of Standards and Technology and University of Colorado, Boulder, Colorado 80309, USA*
[2]*Department of Chemistry and Biochemistry, University of Colorado, Boulder, Colorado 80309, USA*
[3]*Department of Physics, University of Colorado, Boulder, Colorado 80309, USA*

(Received 8 March 2018; accepted 16 April 2018; published online 4 May 2018)

The combination of a pulsed supersonic slit-discharge source and single-mode difference frequency direct absorption infrared spectroscopy permit first high resolution infrared study of the iodomethyl (CH_2I) radical, with the CH_2I radical species generated in a slit jet Ne/He discharge and cooled to 16 K in the supersonic expansion. Dual laser beam detection and collisional collimation in the slit expansion yield sub-Doppler linewidths (60 MHz), an absolute frequency calibration of 13 MHz, and absorbance sensitivities within a factor of two of the shot-noise limit. Fully rovibrationally resolved direct absorption spectra of the CH_2 symmetric stretch mode (ν_2) are obtained and fitted to a Watson asymmetric top Hamiltonian with electron spin-rotation coupling, providing precision rotational constants and spin-rotation tensor elements for the vibrationally excited state. Analysis of the asymmetric top rotational constants confirms a vibrationally averaged planar geometry in both the ground- and first-excited vibrational levels. Sub-Doppler resolution permits additional nuclear spin hyperfine structures to be observed, with splittings in excellent agreement with microwave measurements on the ground state. Spectroscopic data on CH_2I facilitate systematic comparison with previous studies of halogen-substituted methyl radicals, with the periodic trends strongly correlated with the electronegativity of the halogen atom. Interestingly, we do not observe any asymmetric CH_2 stretch transitions, despite $S/N \approx 25{:}1$ on strongest lines in the corresponding symmetric CH_2 stretch manifold. This dramatic reversal of the more typical 3:1 antisymmetric/symmetric CH_2 stretch intensity ratio signals a vibrational transition moment poorly described by simple "bond-dipole" models. Instead, the data suggest that this anomalous intensity ratio arises from "charge sloshing" dynamics in the highly polar carbon-iodine bond, as supported by *ab initio* electron differential density plots and indeed consistent with observations in other halomethyl radicals and protonated cluster ions. *Published by AIP Publishing.* https://doi.org/10.1063/1.5028287

I. INTRODUCTION

Halogen substituted methyl species play significant roles in a range of atmospheric processes, ranging from alkene chemistry[1,2] to ozone depletion.[3] These species are also crucial in important technical applications, such as semiconductor device manufacturing,[4] fire suppression,[5,6] and refrigeration. However, these halogen substituted methyl analogs are of interest in their own right for the new fundamental insights they can offer into the behavior of simple hydrocarbon radicals. Specifically, the halogen atom electronegativity influences a range of molecular properties, including the degree of sp^3 vs. sp^2 hybridization of the central carbon atom as well as the magnitude of the carbon-halogen bond stretching force constant. As one example, the CX bond force constant is known to decrease systematically along the periodic series CH_2Cl,[7] CH_2Br,[8] and CH_2I.[9] Such trends reflect the impact of decreasing electronegativity for the halogen atom, for which decreased "back bonding" with the radical carbon center weakens the force constants for these species.

For methyl radicals (CH_3) and the analogous monohalogen substituted methyl radicals (CH_2F, CH_2Cl, CH_2Br, and CH_2I), electronegativity has a similarly strong impact on planarity and out-of-plane bending anharmonicity. For example, the methyl radical (with the least electronegative H atom substituent[10]) exhibits a relatively harmonic bending mode with a vibrationally averaged planar equilibrium geometry. On the other hand, CH_2F, with the most highly electronegative F substituent, exhibits the least harmonic bending mode with a non-planar double-minimum potential (see the potential energy calculations by Whitney *et al.*[11] and Marshall *et al.*[12]). Such systematic variations in the potential surface reflect the influence of electronegativity and electron withdrawal on the sp^2 vs. sp^3 hybridization of the central carbon radical.

The CH_2I radical has also gained much recent attention as an important player in fundamental atmospheric and tropospheric chemistry, in particular, as an efficient precursor for the formation of "Criegee intermediates" such as CH_2OO radicals. The important class of transient radicals was first proposed in

1947 as an important collision complex in reactions between ozone and unsaturated hydrocarbons,[13] but direct observation of these molecules was not reported until 2008.[14] In 2012, Welz *et al.*[15] provided unambiguous evidence that they had generated the simplest Criegee intermediate using the following bimolecular displacement reaction:

$$CH_2I + O_2 \rightarrow CH_2OO + I, \quad (1)$$

with the CH_2I radical initially produced by UV photodissociation of CH_2I_2. The reaction described in Eq. (1) and other parallel CH_2I reactions, such as

$$CH_2I + O_2 \rightarrow HCHO + IO, \quad (2)$$

are believed to represent important atmospheric pathways for producing highly reactive species that initiate catalytic ozone depletion, influence olefinic concentrations, and produce cyclic hydrocarbon compounds.[1,2] Such iodine chemistry is particularly important in the marine boundary-layer environment, where methylene iodide (CH_2I_2) is generated by marine organisms, enters the atmosphere, and is quickly photodissociated by ultraviolet solar radiation (at wavelengths below 300 nm[16]) into $CH_2I + I$.

The prototypical CH_3 radical (i.e., CH_2X with X = H) was first observed in the vacuum ultraviolet[17] and then later via electron spin resonance spectroscopy.[18] Condensed phase infrared (IR) spectra of methyl radicals have been extensively studied by matrix isolation methods.[19–23] In the gas phase, a vibrationally averaged structure has been determined to be planar,[24] with a rovibrational structure in the CH stretch spectral region studied via high resolution infrared (IR) absorption[25] and Raman photofragment spectroscopy.[26] Additional gas phase IR studies include probing the out-of-plane[27] and in-plane[28] bending modes. A deuterated methyl radical has also been studied in the gas phase at IR frequencies.[27,29]

The halogen-substituted methyl radical analogs have also been intensively studied. The CF_3 radical is known to exhibit a *non-planar*, pyramidal structure in its ground state,[30–32] whereas high-resolution microwave and IR studies suggest that CH_2F has a vibrationally averaged, *planar* ground state structure.[11,33] As noted above, this difference in equilibrium geometry between CF_3 and CH_2F species reflects the degree of sp^2 versus sp^3 hybridization for the central carbon atom, which influences the out-of-plane inversion potential. Other CH_2X molecules have been studied at high resolution, including CH_2Cl, whose rotational structure was investigated in both the microwave[34] and the IR regime,[35] and CH_2Br, whose pure rotational structure has been studied via microwave spectroscopy.[36,37]

Three of the six CH_2I radical vibrational modes—the HCH bend, the CH_2 symmetric stretch, and the CI stretch mode—have been studied while immobilized in a cold argon matrix.[9] Most relevant in this respect is the microwave and millimeterwave study of ground vibrational level rotational structures of CH_2I by Bailleux *et al.*[38] who report ground state rotational constants to high precision, including quartic and sextic centrifugal distortion terms, spin-rotation parameters, and hyperfine coupling constants arising from both the iodine and the hydrogen (*ortho* coupled, $I_H = 1$) nuclei. Bailleux *et al.* concluded that CH_2I has a planar geometry, averaged over zero-point out-of-plane CH_2 wagging motion. They determined the ground electronic state to be of $^2B_1$ symmetry and found that the largest contribution to the hyperfine structure originates from coupling of the quadrupole moment of the radical with the iodine nucleus, in part due to the high nuclear spin angular momentum ($I_I = 5/2$) of ^{127}I. In preparation for the studies reported herein, we have undertaken *ab initio* calculations of CH_2I using density functional theory (DFT) with a variety of available basis sets.[39] The resulting prolate asymmetric top equilibrium structure of CH_2I is illustrated in Fig. 1, with the unpaired electron occupying a p_π orbital along the CI axis. Out-of-plane bending is characterized by an inversion angle θ, whose vibrationally averaged value is zero, and ϕ denotes the azimuthal angle between the CH bond and the CI symmetry axis.

In the experimental work reported herein, we use nonlinear difference frequency generation between two single-mode visible lasers to search for the infrared $v = 1 \leftarrow 0$ symmetric and asymmetric stretch CH_2 bands. We successfully observed the symmetric CH_2 stretch band, with a good signal to noise ratio (S/N ≈ 25:1) for the strongest transitions. For the symmetric stretch band, the spin–rotation fine structure is fully resolved and analyzed. A hyperfine structure is also observed at low angular momentum states, dominated by coupling between electron spin (S = ½) and iodine nuclear spin ($I_I = 5/2$). The net hydrogen nuclear spin is either $I_H = 0$ for the singlet para state or $I_H = 1$ for the triplet ortho state, with hyperfine structures due to the triplet state contributing to broadening of spectral features observed at low total J. It is worth noting that the combination of jet cooling and sub-Doppler resolution in the slit jet expansion geometry permits substantially complete sequential resolution of *rovibrational*, *fine*, and even *hyperfine* structures, which is quite unusual for studies in the near infrared region of the spectrum.

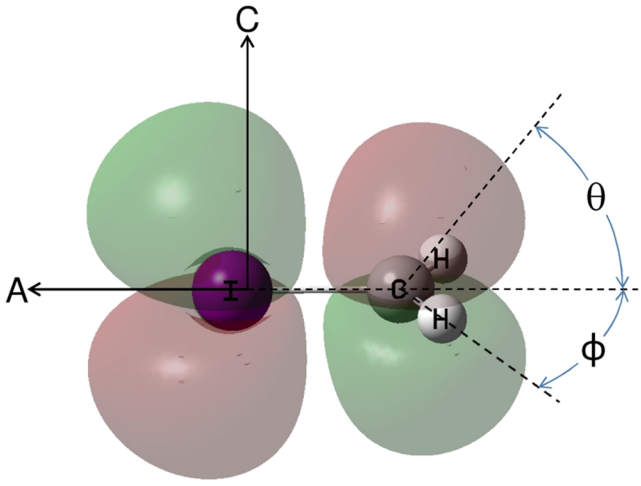

FIG. 1. Representation of the CH_2I equilibrium structure as determined with a DFT/B3LYP calculation. The p_π orbital of the unpaired electron is illustrated above and below the molecular plane. The *a* and *c* principal rotation axes are labeled (the *b* axis is roughly out of the page). The inversion angle is θ, and the angle between the symmetry axis and the C–H bond is ϕ.

The organization of this paper is as follows. Methods for obtaining first high resolution spectra of supersonically cooled CH_2I radicals are described in Sec. II, with fully resolved rovibrational and spin-rotation structures for the K_a: $0 \leftarrow 0$ and $1 \leftarrow 1$ transitions presented in Sec. III and analyzed with a Watson spin-rotation Hamiltonian. Section IV discusses how these results inform our understanding of the potential energy and dipole moment surfaces for CH_2I and other halomethyl radical species, with concluding comments summarized in Sec. V.

II. EXPERIMENT

The supersonic slit-discharge molecular beam source and IR difference frequency spectrometer have been described in detail elsewhere.[40] Briefly, the success of the experiment depends on the high absorbance sensitivity and precision frequency control arising from several factors: (1) high radical density per quantum state, (2) sub-Doppler linewidths ($\Delta\nu \approx 0.002$ cm^{-1}), (3) long effective absorption path length, (4) highly stable, broadly tunable IR sources, and (5) detection sensitivity near the quantum shot-noise limit. The first three contributions are the consequence of operating an intense supersonic *slit*-discharge pulsed beam source *in vacuo* inside of a multipass Herriott cell.[41] The fourth and fifth contributions are provided by active servo loop stabilized single-mode difference-frequency laser generation and aggressive reduction of common mode technical noise with fast subtraction electronics.

Figure 2 shows a cross section of the supersonic slit-discharge pulsed molecular beam source and the multipass Herriott cell. The CH_2I radical is produced by bubbling diluent carrier gas through temperature controlled CH_2I_2 to achieve near saturation (≈1 mbar) partial pressure concentrations in the vapor phase. The CH_2I_2 radical precursor is then delivered to the slit jet at a stagnation pressure of 250 mbar and a fractional precursor concentration of 0.4%, with a carrier gas mixture of 62% neon, 22% helium, and 5% hydrogen. The Ne:He ratio

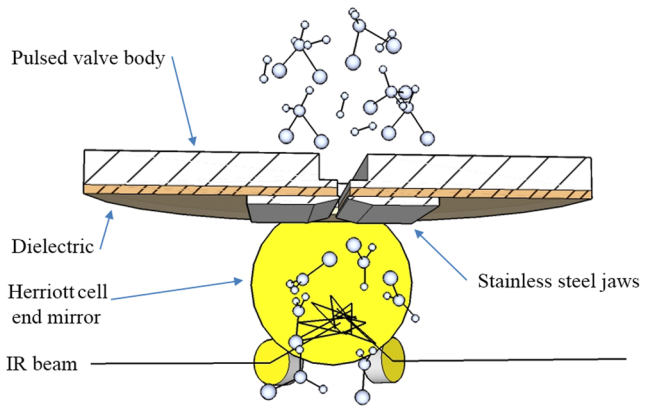

FIG. 2. Cross section of the supersonic slit-discharge pulsed valve. A rare-gas/H_2/CH_2I_2 mixture flows into the stagnation region behind the slit valve, with a solenoid valve and gasket sealing/unsealing a rectangular slit aperture (40 mm × 300 μm) with a 19 Hz duty cycle to produce gas pulses of ≈1 ms duration. A 1 mm thick dielectric is sandwiched between the pulsed valve body and stainless steel jaws. The discharge is struck by grounding the body of the pulsed valve and applying a –600 V square wave to the jaws at 50 kHz, with peak currents of order 100–1000 mA and peak current densities of 8-80 A/cm^2.

is chosen to achieve stable discharge characteristics, low discharge infrared background, and narrow sub-Doppler velocity distributions in the slit supersonic expansion, with hydrogen added to chemically optimize CH_2I radical production. The slit expansion geometry is 40 mm × 300 μm and produces sub-Doppler linewidths along the long axis of the slit of 60 MHz (0.002 cm^{-1}) FWHM in the 3000 cm^{-1} CH stretch spectral region. The slit supersonic expansion rapidly cools the CH_2I rotationally to approximately 16 K (as measured from a rotational Boltzmann analysis) with significant but likely less aggressive cooling of the vibrational degrees of freedom. The pulsed valve operates at 19 Hz with a duration of approximately 1 ms and a 1.9% duty cycle.

CH_2I_2 is converted into CH_2I radicals in a discharge formed by applying a 6.0 kV/cm square wave between the pulsed-valve slit aperture and a set of steel jaws separated by a thin 1 mm insulating polymer to establish a 300 μm slit width. This discharge is modulated at 50 kHz for phase sensitive detection, with peak discharge currents of about 270 mA. There are two primary reaction pathways for producing CH_2I radicals: (1) dissociative attachment of the CI bond by free electrons contained within the discharge,

$$CH_2I_2 + e^- \rightarrow CH_2I + I^-, \tag{3}$$

and (2) abstraction of I atoms by atomic hydrogen generated within the discharge,

$$CH_2I_2 + H \rightarrow CH_2I + HI, \tag{4}$$

with both reactions likely contributing to the absorbance signal under the present experimental conditions.

Narrow band IR radiation is produced via difference frequency generation between two single mode visible lasers, a ring dye laser and an etalon-narrowed single mode Ar^+ laser, in a 40 mm long, periodically poled and thermally phase matched MgO:$LiNbO_3$ periodically poled lithium niobate (PPLN) crystal.[42,43] The dye laser operates with a Rhodamine 590 dye to produce 200 mW, with the Ar^+ laser 514.5 nm line generating about 300 mW. Difference frequency generation of the two beams produces 10-20 μW of IR radiation with <1 MHz (<3×10^{-5} cm^{-1}) linewidth which is broadly tunable between 2600 cm^{-1} and 3500 cm^{-1}.

The IR beam is split into two beams, with half the power directed to a liquid-nitrogen cooled InSb *reference* detector and the remaining IR beam making 16-passes (4 cm slit, 64 cm path length) through the throat of the slit-discharge pulsed molecular beam source, as illustrated in Fig. 2. After exiting the Herriott cell, the IR radiation is focused onto an InSb *signal* detector. The signal beam is corrected for laser amplitude noise by a fast subtraction circuit (>30 dB reduction in common mode noise from 10 kHz to 1 MHz) and phase sensitively detected with a lock-in amplifier circuit to extract 50 kHz absorption signals due to the modulated radicals. The demodulated signal is then digitized by a fast analog-to-digital (A/D) converter and boxcar integrated to achieve additional background subtraction in the time domain. This arrangement achieves an rms absorbance noise ($1.5 \times 10^{-6}/\sqrt{\text{Hz}}$) within a factor of two of the shot noise limit, which yields signal-to-noise ratios of 25:1 on optimal symmetric stretch absorption lines.

The high IR frequency stability and reproducibility are obtained by referencing both single-mode lasers to a Fabry-Pérot interferometer and a traveling Michelson interferometer wavemeter, both of which are referenced to a frequency stabilized HeNe laser. The Fabry-Pérot cavity has a 250 MHz free spectral range, with a length actively controlled by locking to a frequency stabilized HeNe laser, as described by Riedle *et al.*[44] The single-mode Ar^+ laser, in turn, is locked to a different fringe of the same Fabry-Pérot cavity, effectively transferring the stability of the HeNe laser to the Ar^+ laser. The dye laser frequency is determined by recording fringes transmitted through the stabilized Fabry-Pérot cavity, yielding an IR frequency reproducibility of ±12 MHz or ±3.9 $\times 10^{-4}$ cm^{-1}. Absolute IR frequencies are referenced to known R(2) methane lines in the ν_3 asymmetric stretch manifold,[45] which are determined in the slit jet to an uncertainty of ±6 MHz (±2 $\times$ 10^{-4} cm^{-1}) by Gaussian fits to the absorption profiles. The net result is an absolute frequency accuracy of ±13 MHz (±4.5 $\times$ 10^{-4} cm^{-1}) for each sub-Doppler limited spectral feature.

Such high resolution direct absorption studies also provide a novel opportunity for the direct measurement of the absolute radical number densities for highly reactive species. To implement such Beer's law estimates (i.e., $A = [N]\sigma_{eff}l$), one requires (i) an assigned spectrum of experimental fractional absorbances (A), (ii) integrated IR absorption intensities (S_0) which can be reliably predicted from *ab initio* calculations described in Sec. III, (iii) measured sub-Doppler linewidths ($\Delta\nu$) and effective absorbance cross sections ($\sigma_{eff} \approx S_0/\Delta\nu$), and (iv) the path length (ℓ) of the probe laser through the Herriott cell slit discharge expansion region. Combining experimentally obtained column integrated absorbances, the laser path length, and the calculated S_0 = 3.9 km/mol, one estimates the total CH_2I radical density (summed over all quantum states) to be 9.6×10^{12} radicals/cm^3 for a probe laser position 10 slit widths (3 mm) downstream from the slit aperture. This translates into an even higher density of $\approx 1.0 \times 10^{14}$ radicals/cm^3 at the slit jet orifice, which underscores the efficiency of both Langevin electron dissociative attachment to and H atom abstraction from the methylene iodide precursor, as well as the remarkable densities of transient species that can be formed in a 1D supersonic discharge expansion.

III. RESULTS AND ANALYSIS

The frequency range of our apparatus provides the opportunity to observe two CH stretching modes in CH_2I: the a-type CH_2 symmetric stretch and the b-type CH_2 asymmetric stretch. The infrared frequency regions searched have been guided by *ab initio* theory. In particular, Gaussian 09 DFT/B3LYP calculations with AnZP (n = 3, 4, 5) basis sets[46] provide harmonic band origins that are scaled by 0.9637 ± 0.0031 to estimate the corresponding anharmonic values (see the work of Dong *et al.*[47]). These harmonic calculations with the highest quality (AQZP) basis set predict a symmetric stretch band origin at 3056 ± 10 cm^{-1}. By way of additional confirmation, anharmonic Gaussian 09 *ab initio* calculations yield predictions of 3042 cm^{-1} for the symmetric stretch band origin. Based on both scaled harmonic and anharmonic CH stretch values from B3LYP/AQZP calculations as the best guide, we also predict the asymmetric stretch band origin to be somewhere in the 3151 cm^{-1} to 3186 cm^{-1} window.

A. The CH_2 symmetric stretch mode

High resolution searches initiated in the 3040 cm^{-1} symmetric stretch region quickly revealed lines attributable to the CH_2I radical. After optimization of conditions for CH_2I radical production in the slit discharge, high-resolution IR absorption data for the symmetric stretch band were then collected over the 3039-3055 cm^{-1} frequency range at 12.5 MHz (4.17 $\times$ 10^{-4} cm^{-1}) intervals, with all assigned spectral features measured independently in three separate scans to improve the statistics. An overview scan of the *a*-type symmetric stretch band (ΔK_a = even, ΔK_c = odd) is displayed in Fig. 3. The data are averaged over a time window of 4 ms per frequency increment except between 3045.7 cm^{-1} and 3048 cm^{-1}, where the averaging is increased 4-fold per frequency point to improve S/N on the iodine nuclear hyperfine structure (which is only observed for transitions out of the lowest N = 0, 1, and 2 rotational states).

The most prominent features in Fig. 3 belong to the K_a: 0 ← 0 progression. Figure 3 also includes a spectral simulation based on a 16 K rotational temperature and 60 MHz linewidths, with rotational constants obtained from the fits reported in Sec. III B. Despite a large A constant (≈9 cm^{-1}) on the order of kT_{jet}, *a*-type progressions in K_a: 1 ← 1 are also evident in the symmetric stretch band, as well as fully resolved doublets due to spin-rotation splitting in both the K_a = 0 and 1 lower states. These details are further illustrated in an expanded 1.5 cm^{-1} spectral window of the R branch (see Fig. 4), which clearly

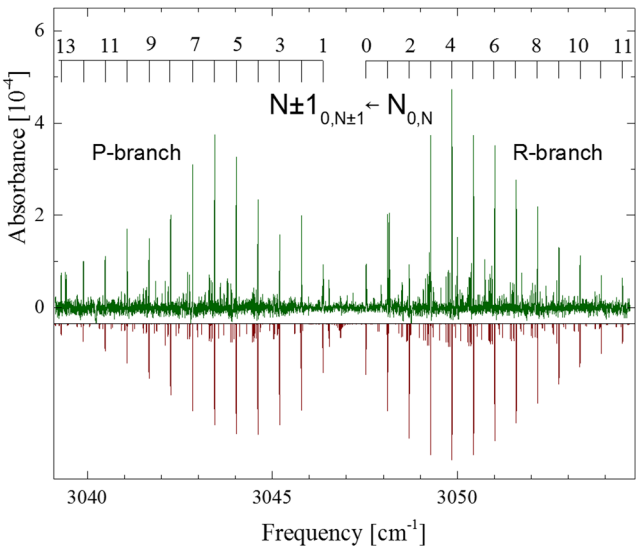

FIG. 3. Upper panel: The CH_2 symmetric stretch transition from the ground state (v = 0) to the first excited (v = 1) vibrational state. The most prominent progression (K_a: 0 ← 0) is labeled with N, the ground-state rotational quantum number. Averaging is 4 ms per point, except between 3045.7 cm^{-1} and 3048.0 cm^{-1} where the averaging is increased 4-fold to observe the hyperfine structure at low N values. Lower panel: PGOPHER spectral simulation assuming a 16 K rotational temperature and 60 MHz linewidth.[48,49] Rotational constants used in the simulation are those reported in Sec. III B.

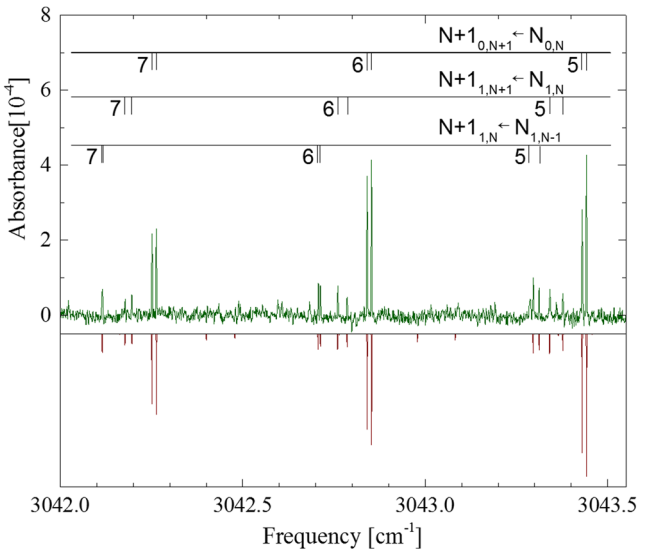

FIG. 4. Upper panel: A detailed section of the CH_2 symmetric stretch R branch. The K_a: 0 ← 0 and 1 ← 1 progressions are labeled with N, the ground-state rotational angular momentum quantum number. The spin-rotation splitting is clearly resolved. Lower panel: Simulation assuming a 16 K rotational temperature and 60 MHz linewidth, and spectroscopic constants reported in Sec. III B.

resolves the spin-rotation dynamics in both K_a: 1 ← 1 and K_a: 0 ← 0 progressions. The downward facing spectra in Fig. 4 reflect a simulation based on parameters from a least squares fit, as described in Fig. 3. At our sensitivities, the bands out of the $K_a = 1$ manifold at such low jet temperatures are detectable in spite of the additional 3-fold reduction in population for K_a = odd vs. even states by para:ortho nuclear spin statistics, which arises as a result of the two equivalent ($I = ½$) hydrogen atoms in the CH_2 moiety.

In the interest of completeness, we also searched extensively for the CH_2 asymmetric stretch (b-type band), which as mentioned above, one would expect from scaled harmonic and anharmonic frequency calculations to find in the 3151 cm^{-1} to 3186 cm^{-1} range. For a b-type band of a near prolate top at such low jet temperatures, the most obvious spectral signature will be the K_a: 1 ← 0 Q-branch progression which should be further blue shifted by roughly A ≈ 9 cm^{-1} from the band origin. We therefore searched continuously for this asymmetric stretch absorption band from 3143.8 cm^{-1} to 3212 cm^{-1}, with no signals observable at our current absorbance sensitivity.

In order to extract suitably quantitative upper limits for the missing band intensity, we note from PGOPHER simulations[48,49] that a-type and b-type bands should exhibit features of similar intensities for comparable S_0 integrated intensities. The root-mean-square (RMS) absorbance noise in this region is 2.2 × 10^{-5}, with the feature of greatest intensity in the a-type band (5_{05} ← 4_{04}) having an absorbance of about 8.3 × 10^{-4}. We therefore predict the asymmetric stretch to have an integrated absorbance upper limit that is at least a factor of 25 *smaller* than the symmetric stretch. This seems quite surprising at first, since for a sp^2 hydridized radical center and a 120° HCH bond angle, the simple bond-dipole model would predict a 3-fold *larger* intensity for the asymmetric vs. symmetric stretch bands. Indeed, this is reminiscent of a similar reversal of symmetric vs. asymmetric stretch intensity behavior noted previously in the chloromethyl (CH_2Cl) radical, for which the asymmetric stretch was also too weak to be detected. This provides additional evidence for the influence of vibrationally induced charge transfer in such halomethyl radicals due to a strongly polar CX bond. In essence, such effects arise from the collateral increase (or decrease) in the transition dipole moment due to vibrationally mediated "charge-sloshing" along the polar CX bond, which in turn is caused by normal mode and/or anharmonic coupling of the CX and CH_2 stretch vibrational degrees of freedom.[11,35,50] These issues will be revisited in more detail with *ab initio* calculations in Sec. IV B.

B. Fine-structure interactions and rotational constants

As illustrated in Fig. 4, an additional doublet fine-structure on each of the rovibrational transitions is clearly resolved, with splittings due to coupling between overall rotational end-over-end tumbling angular momentum (N) and the intrinsic spin angular momentum of the unpaired electron (S = 1/2), which by vector addition generates total spin plus rotational angular momentum quantum numbers $\boldsymbol{J} = \boldsymbol{N} + \boldsymbol{S}$. We can quantify the effect of spin-rotation on the overall rotational manifold by considering the rigid-rotor spin-rotation Hamiltonian, $H = H_{rot} + H_{sr}$, or

$$H = \sum_{\alpha} A_{\alpha} J_{\alpha}^2 + \frac{1}{2} \sum_{\alpha,\beta} \varepsilon_{\alpha\beta} (N_{\alpha} S_{\beta} + S_{\beta} N_{\alpha}), \qquad (5)$$

where $\varepsilon_{\alpha\beta}$ are the elements of the spin-rotation tensor, A_{α} represents the A, B, and C rotational constants, and the labels α, β denote the a, b, and c principal rotation axes.[51] For molecules of orthorhombic symmetry, the only non-zero elements of $\varepsilon_{\alpha\beta}$ are along the diagonal, i.e., ε_{aa}, ε_{bb}, and ε_{cc}. Figure 5 illustrates the spin-rotation manifold structure for K_a = 0 and 1

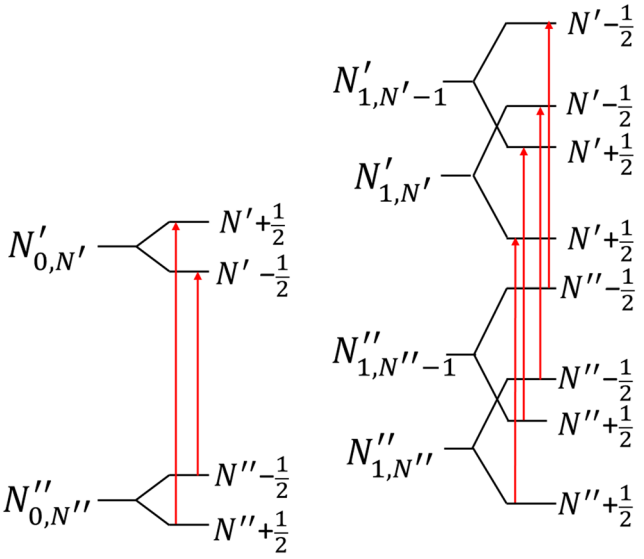

FIG. 5. Energy-level diagram for $K_a = 0$ and 1 transitions, showing the effects of coupling of the molecule's rotational angular momentum (N) with the spin ½ angular momentum of the unpaired electron. The strong ΔJ = ΔN transitions observed in the CH_2I symmetric-stretch absorption spectrum are designated by red arrows.

a-type transitions. Each end-over-end tumbling angular momentum state (N) is split by the electron spin angular momentum into doublets (except for $N = 0$) with the total angular momentum quantum number $J = N \pm 1/2$. Although $\Delta J = 0, \pm 1$ selection rules allow three transitions in the P and R branches (and four in the Q branch), there is a strong propensity for $\Delta J = \Delta N$ transitions being the highest intensity. Thus, the current instrumental sensitivity permits observation of only the two strongest lines corresponding to $\Delta J = \Delta N$ (see Fig. 5).

To compute the $v = 1$ rotational constants, the ground state values are fixed at the microwave spectroscopy values,[38] and the $v = 1$ quartic and sextic centrifugal distortion terms are held at the ground-state microwave values in the A reduction and Ir representation. The upper-state eigenvalues A', B', C', ε_{aa}', ε_{bb}', and ε_{cc}', and the band origin ν_0, are then least squares fit to 36 spin-rotation resolved $K_a = 0$ transitions and 40 spin-rotation resolved $K_a = 1$ transitions. We used two computational approaches for evaluating these spectroscopic constants. The first one involves fitting the spectroscopic data to a rigid, prolate asymmetric top Watson Hamiltonian[52] in a Wang basis set[53] (A-reduction, Ir representation) with the eigenvalues determined by nonlinear weighted least-squares fitting routines from STARPAC.[54] The second approach uses the versatile spectral simulation and least-squares fitting program PGOPHER.[48,49] Both fitting programs agree within their reported statistical uncertainties, with the PGOPHER fit results summarized in Table I. All ground-state spectroscopic constants of Bailleux *et al.*[38] are included as fixed parameters in the fit. As shown in Sec. IV A, hyperfine contributions can be neglected or included by choice of transitions from low N tumbling states in which hyperfine interactions are most cleanly observed. We verify this by comparing ground-state two-line combination differences from our data to simulations using hyperfine-resolved microwave values by Bailleux *et al.* (excluding hyperfine interaction parameters), which reveals negligible deviations for observed vs predicted ground state combination differences above $N' = 3$ and $N' = 6$ for the $K_a = 0$ and $K_a = 1$ progressions, respectively.

TABLE I. Spectroscopic results from a rigid rotor/spin rotation Watson Hamiltonian least squares fit (based on the PGOPHER software in the A reduction and Ir representation) to the CH_2I ($v = 1 \leftarrow 0$) symmetric stretch data, with ground state rotational constants and excited state quartic and sextic centrifugal distortion terms fixed at microwave values[38] ($\sigma = 0.000\,24\ cm^{-1}$). All values are in cm^{-1}, with numbers in parentheses representing uncertainties in the least significant digit.

	Ground state	Symmetric CH_2 stretch
A	9.228 915	9.121 03(5)
B	0.296 756 00	0.296 398 4(11)
C	0.287 312 78	0.286 814 4(11)
Δ_N	$2.544\,39 \times 10^{-7}$	$2.544\,4 \times 10^{-7}$[a]
Δ_{NK}	$8.274\,89 \times 10^{-6}$	$8.274\,9 \times 10^{-6}$[a]
Δ_K	8.089×10^{-4}	8.089×10^{-4}[a]
δ_N	$7.872\,4 \times 10^{-9}$	7.872×10^{-9}[a]
δ_K	$4.678\,9 \times 10^{-6}$	4.679×10^{-6}[a]
ϕ_N	-1.13×10^{-13}	-1.1×10^{-13}[a]
ϕ_{NK}	7.61×10^{-12}	7.6×10^{-12}[a]
ϕ_{KN}	2.92×10^{-10}	2.9×10^{-10}[a]
ε_{aa}	−0.981 004 70	−0.965 3(4)
ε_{bb}	$-3.090\,56 \times 10^{-2}$	$-3.077(2) \times 10^{-2}$
ε_{cc}	$6.965\,12 \times 10^{-3}$	$6.97(2) \times 10^{-3}$
ν_0	...	3046.952 7(6)

[a]In least squares fits to the symmetric stretch excited state spectra, all ground state constants as well as centrifugal distortion constants in the upper state have been fixed at values from the microwave studies of Bailleux *et al.*[38]

IV. DISCUSSION

A. Nuclear spin statistics and hyperfine structure

The rovibrational spectrum of CH_2I reveals the effects of nuclear spin in two ways: (i) nuclear spin statistics due to the exchange of two identical hydrogen atoms and (ii) nuclear hyperfine structures arising from coupling between the nuclear spin and the rotation plus electron-spin angular momentum, as well as iodine quadrupolar interactions with the electric field gradient at the iodine nucleus. The nuclear spin statistics arise from the required antisymmetry of the total wavefunction for exchange of two indistinguishable fermions ($I = ½$). With respect to such H atom exchange (topologically equivalent to a 180° rotation about the a axis), the angular momenta of the two identical H nuclei must couple to yield either nuclear spin *triplet* eigenstates of even symmetry ($|\uparrow\uparrow\rangle, \frac{1}{\sqrt{2}}(|\uparrow\downarrow\rangle + |\downarrow\uparrow\rangle), |\downarrow\downarrow\rangle$) or nuclear spin *singlets* of odd symmetry ($\frac{1}{\sqrt{2}}(|\uparrow\downarrow\rangle - |\downarrow\uparrow\rangle)$). The electronic wavefunction is always odd due to a half filled p_π orbital on the C atom, the ground state vibrational wavefunction is always even, and the rotational wavefunction is symmetric (antisymmetric) with respect to π rotation for even (odd) values of K_a. Since the total wavefunction must be antisymmetric, this requires that eigenstates associated with $K_a = 0, 2, 4, \ldots$ and $K_a = 1, 3, 5, \ldots$ couple with the triplet and singlet nuclear-spin eigenstates, respectively. The same reasoning applies to the symmetric stretch excited state of A_1 symmetry, thus predicting a statistical ratio of 3:1 for even:odd K_a levels.

The intensities of individual rovibrational transitions in an absorption band vary according to

$$S_0 = N_0 l g_{NS}(K_a) g_J g_K A(J', J'') e^{-\frac{E_{rot}(v'', J'')}{kT}} |\langle \psi'_{vib} | \boldsymbol{\mu} | \psi''_{vib} \rangle|^2, \quad (6)$$

where N_0 is the population of the ground vibrational state, ℓ is the absorption path length, $g_{NS}(K_a)$ is the nuclear spin weight for a particular K_a, $g_J = 2J + 1$ is the m_J degeneracy, g_K is the angular momentum projection degeneracy, $A(J',J'')$ is the Hönl-London factor, $E_{rot}(v'',J'')$ is the energy of the ground ro-vibrational state, kT is the thermal energy associated with rotation, ψ'_{vib} and ψ''_{vib} are the excited- and ground-state vibrational wavefunctions, and $\boldsymbol{\mu}$ is the transition dipole operator. The natural logarithm of Eq. (6) predicts a linear Boltzmann relationship between $\ln[S/g_K g_J A(J', J'')]$ and $E_{rot}(v'',J'')$, which is presented in Fig. 6 for both P and R branches of the CH_2I symmetric CH stretch band. Data for both $K_a = 0 \leftarrow 0$ and $K_a = 1 \leftarrow 1$ progressions nicely satisfy the Boltzmann expectations for a linear plot with a slope of $-1/kT$ and a y-intercept of $\ln[N_0 l g_{NS}(K_a) |\langle \psi'_{vib} | \boldsymbol{\mu} | \psi''_{vib} \rangle|^2]$.

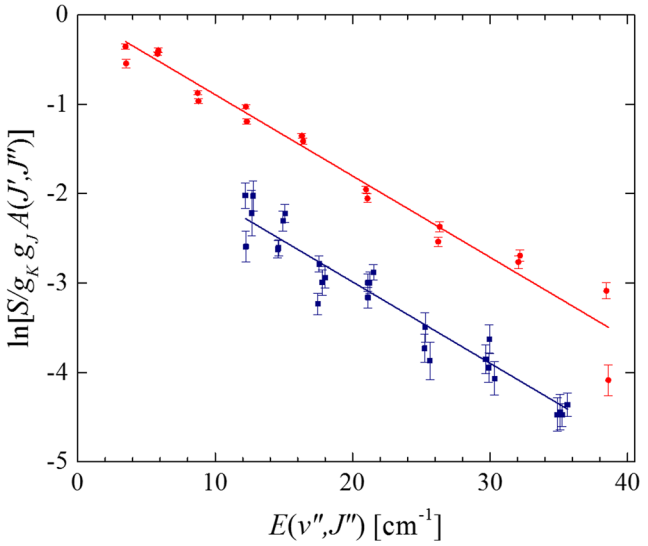

FIG. 6. Boltzmann plot of the CH_2I symmetric stretch P and R branches. Data from the $K_a = 0$ and $K_a = 1$ progressions are shown as red circles and blue squares, respectively, with solid lines representing the least-square fit. Both progressions yield the same slopes within uncertainty and thus are least squares fit to a common rotational temperature ($T_{rot} = 15.8 \pm 0.5$ K). The data are normalized such that the $K_a = 0$ y-intercept is zero, yielding a ratio of H atom nuclear spin statistical weights of $g_{NS}(0)/g_{NS}(1) = 3.15 \pm 0.13$. This value is in excellent agreement with the 3:1 ortho to para nuclear spin ratio anticipated for an identical pair of H atoms in CH_2I.

Furthermore, we expect all the radicals to be equilibrated to the same rotational temperature (i.e., the slope of Boltzmann plot), as is confirmed by independent least squares linear fits to these $K_a = 0$ and 1 transitions; we therefore fit both rotational progressions simultaneously to the same slope, allowing the y-intercepts to float independently. This results in a rotational temperature of 15.8 ± 0.5 K which is consistent with several previous spectroscopic studies of neutral radicals in the slit-discharge spectrometer. The y-intercepts yield a ratio of the nuclear spin degeneracies to be $g_{NS}(0)/g_{NS}(1) = 3.15 \pm 0.13$ which is also consistent with the *unrelaxed* nuclear-spin weights of 3:1. As one interesting take-home message, the data clearly indicate that there is still insufficient time in the slit jet expansion for collisional equilibration between nuclear spin states, even for (i) open shell species, (ii) the much slower density drop off ($\rho \propto 1/r$) and thus much higher collision numbers of a 1D slit jet expansion, and (iii) molecules with high atomic number constituents such as iodomethyl radicals.

Nuclear spin effects can also become evident by way of hyperfine structures in the spectra, which, although typically with such small frequency splittings as to be only accessible by microwave studies, is indeed detectable in the near infrared due to the sub-Doppler resolution capabilities achievable in a slit jet expansion. For the iodomethyl radical, such a structure is only resolvable for transitions out of the very lowest N, K_a, K_c states, for which the vector difference between the total (**F = N + S + I**) and end-over-end tumbling (**N**) angular momenta can become appreciable. For the present slit expansion geometry, hyperfine structures for the symmetric stretch of CH_2I becomes observable for $N'' \leq 2$ in the $K_a = 0 \leftarrow 0$ progressions and $N'' \leq 5$ for the $K_a = 1 \leftarrow 1$ progressions. Indeed, the vanishing of such additional hyperfine splittings in the infrared spectra is what permitted us to fit spectral data at higher rotational levels to a simpler rigid-rotor/spin-rotation Hamiltonian, neglecting structures due to nuclear hyperfine effects (as described in Sec. III B).

At sufficiently low N'', however, the hyperfine structure clearly becomes partially resolvable. By way of example, the top panel of Fig. 7 shows a detailed spectrum of the $1_{01} \leftarrow 0_{00}$ transition. Here, the iodine nuclear spin ($I_I = 5/2$) dominates the hyperfine structure in the ground vibrational state via the iodine nuclear quadrupole moment. According to Bailleux *et al.*,[38] the iodine nuclear quadrupole coupling is two orders of magnitude larger than the hydrogen Fermi contact interaction. This predominance of iodine in the hyperfine structure is evident in the energy level patterns in Fig. 7 (see inset) which show (sequentially from left to right) (i) the coupling of **N** with **S** to yield **J**, followed by (ii) coupling of **J** with $\mathbf{I_I} = 5/2$ to make $\mathbf{F_1}$, and then, finally (iii) the coupling of $\mathbf{F_1}$ with $\mathbf{I_H}$ to make the total angular momentum **F**. Specifically, the iodine hyperfine lines (labeled a-f) are all well resolved, with much weaker contributions due to the hydrogen Fermi contact interactions that are unresolved at our 60 MHz resolution, but clearly still contribute to a slight broadening of the spectral features.

The spectral simulation in the bottom panel of Fig. 7 shows a stick diagram of all the hyperfine transitions for $1_{01}(J', F_1', F') \leftarrow 0_{00}(J'', F_1'', F'')$ predicted by coupling the J, I_I, and I_H angular momenta, as well as a convolution

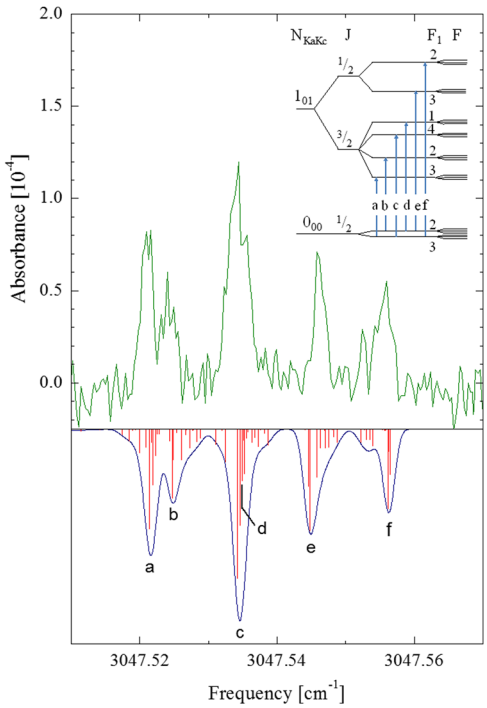

FIG. 7. Upper panel: Sample experimental scan over the $1_{01}(J', F_1', F') \leftarrow 0_{00}(J', F_1'', F'')$ transition revealing a partially resolved hyperfine structure. Lower panel: Predicted hyperfine spectrum (red stick plot) and the corresponding convolution (blue line) over a 60 MHz experimental linewidth. **a**–**f** represent transitions between hyperfine levels arising from coupling of $\mathbf{J} = \mathbf{N} + \mathbf{S}$ to the iodine nuclear spin, $\mathbf{I_I}$. Inset: Energy levels arising from spin-rotation and sequential hyperfine coupling of $\mathbf{J} = \mathbf{N} + \mathbf{S}$ to both $\mathbf{I_I}$ and $\mathbf{I_H}$. The less pronounced hyperfine structure due to additional coupling with $\mathbf{I_H}$ is not resolved but does contribute to broadening of the sub-Doppler lines.

of the stick spectrum with our 60 MHz sub-Doppler instrumental linewidth. This simulation in Fig. 7 is based on least squares fitted values for the vibrationally excited state obtained from rovibrational/spin rotation spectroscopic analysis of the present work (as reported in Table I), along with the ground state hyperfine constants of Bailleux *et al.*[38] which are assumed to be the same in the vibrationally excited state. The agreement between the experimental and predicted spectral hyperfine structure is clearly extremely good. It is worth noting that the ability to resolve such levels of hyperfine detail is quite unusual for infrared spectroscopy (particularly for highly reactive radical species) and made possible only by sub-Doppler capabilities intrinsic to the slit jet expansion geometry.

B. Asymmetric vs. symmetric stretch IR intensities: "Charge-sloshing" effects

Closely related to planarity of the molecule and the electronegativity of the substitution atom is the strength of the asymmetric-stretch infrared intensity relative to that of the symmetric stretch. As stated in Sec. III A, we searched for the asymmetric stretch band over a wide spectral range (3143.8 cm^{-1} to 3212 cm^{-1}) and found it to be at least 25-fold weaker than the corresponding symmetric stretch. The transition strength of any particular vibrational mode depends, to first order, on how the dipole moment, $\boldsymbol{\mu}(Q) = \sum_i q_i \boldsymbol{r}_i$, changes with respect to the relevant normal mode coordinate Q, where q_i is the charge distribution and $\boldsymbol{r}_i$ is the effective charge separation. The so-called transition dipole moment, $\partial\boldsymbol{\mu}/\partial Q$, contains two terms: (1) $\sum_i q_i(\partial \boldsymbol{r}_i/\partial Q)$, the change of the dipole moment due to the change of the effective charge separation, and (2) $\sum_i (\partial q_i/\partial Q)\boldsymbol{r}_i$, the change of the dipole charge distribution. The first term corresponds to the so-called bond-dipole model, where the charge distribution along the bond axis is assumed to be constant and the transition dipole moment depends on the change of the bond length due to the excitation of an anharmonic oscillator, i.e., the change of the effective charge separation due to the new geometry induced by the transition. Given a H–C–H bond angle, it is straightforward to compute the bond-dipole model prediction for the ratio of the asymmetric to symmetric stretch intensities. For a pure sp^2 hybridization of the central C and a $2\phi = 120°$ HCH bond angle, the bond-dipole model predicts an intensity ratio of $I_{asym}/I_{sym} = \tan^2(\phi) = 3/1$. Figure 8 plots the available asymmetric to symmetric stretch intensity ratios for all substituted methyl radicals under discussion, none of which match the simple bond-dipole expectations. The closest is CH_2D, with a ratio of 1.9 ± 0.2,[29] followed by CH_2F, with a ratio of 0.55 ± 0.06.[11] Note that for both CH_2Cl[35] and CH_2I radicals, the asymmetric-stretch modes were not detected and thus the values plotted in Fig. 8 reflect the experimental upper limits.

The bond-dipole model fails to predict accurate intensity ratios in these substituted halomethyl radicals because it ignores shifts in the dipolar charge distribution with stretching of the molecular bond. This effect has been given the descriptive name "charge sloshing." Indeed, Whitney *et al.*[35] first proposed this charge-sloshing motif in spectroscopic studies

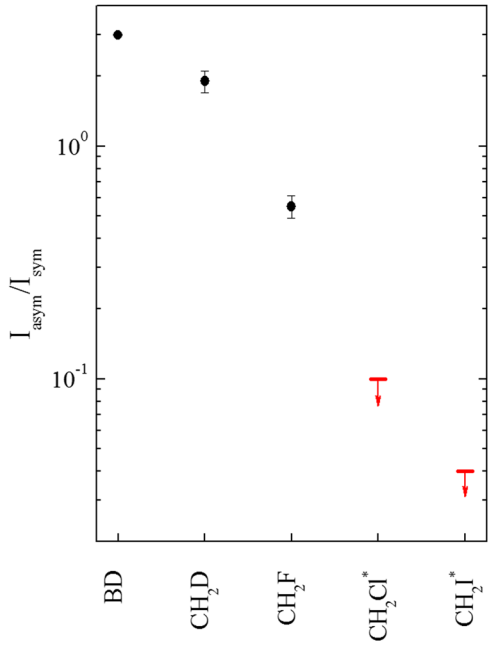

FIG. 8. Ratios of asymmetric stretch IR intensity to symmetric stretch IR intensity for CH_2X. The values for CH_2Cl and CH_2I represent the experimentally determined upper limits. Note that the experimental values are all much lower than the 3:1 ratio predicted from the bond dipole (BD) model but could be consistent with an intensity enhancement for the symmetric stretch by "charge-sloshing" effects noted in previous radical and molecular ion spectroscopy studies.[11,35,50,55–57]

of CH_2Cl, which at the time was ascribed to additional electron flows along the strongly polar CCl bond upon symmetric stretching of the CH bond. The electron flow along the CH bond is predominantly from the H to the C atom. This charge sloshing effect adds constructively and can therefore enhance the symmetric stretch IR intensity by many folds over the bond-dipole contributions. Conversely, the asymmetric CH stretch excitation has by symmetry a vanishing component of the dipole transition moment along the C–Cl bond axis, which therefore precludes a similar enhancement mechanism. There have been several examples of such a "charge sloshing" paradigm playing a major role in halides, hydronium ions, and water complexes, as nicely elucidated by McCoy, Johnson, and co-workers.[50,55–57]

We can address this issue quantitatively by looking at differential charge density maps in the relevant *ab initio* wavefunctions. Toward this end, we have performed a series of *ab initio* calculations at the B3LYP/AnZP (n = 3,4) level[46] for CH_2X (X = D, F, Cl, Br, and I), optimizing the equilibrium geometries and calculating the symmetric/asymmetric CH stretch normal mode coordinates. We then performed a second set of calculations for these same molecules at a fixed normal mode displacement ($Q = 0.1$) along each of the symmetric and asymmetric CH stretch coordinates, subtracting the vibrationally excited and equilibrium electron densities at the wavefunction level. The quality of the *ab initio* method/basis set is held constant throughout this series of methyl radicals, which we choose to be at the B3LYP/AQZP level due to the more limited options for the heavy iodine atoms. To achieve uniformity across this suite of comparisons, we also maintain C_s symmetry to reflect the vibrationally averaged

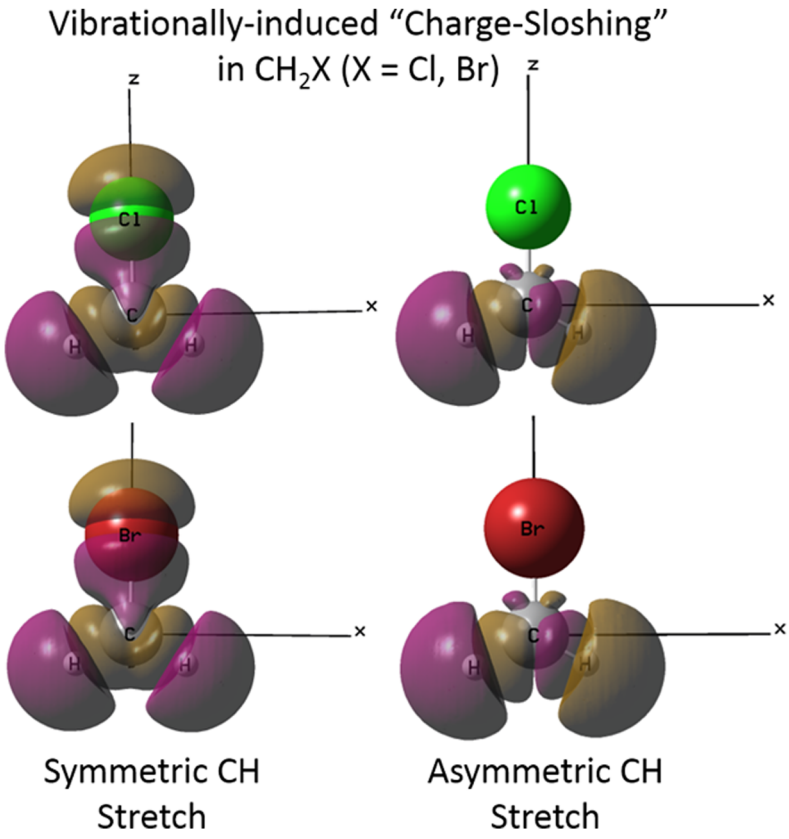

FIG. 9. Wavefunction differential charge densities for CH_2X (X = Cl, Br) between (i) $Q = 0.1$ excitation of the symmetric and asymmetric CH stretching modes and (ii) the equilibrium geometry (red/gold represent the increase/decrease of electron density). Calculations are done in Gaussian 09 using density functional theory (B3LYP) in an AQZP basis set.[39] Note the significant flow of electron density ("charge sloshing") outward along the CCl and CBr bond axes for the symmetric vs. asymmetric CH stretch excitation (see the text for details).

planar geometry for all species. Plotted as signed isocontours of charge difference probability in Fig. 9, these charge difference density plots serve to highlight both the sign and appreciable magnitude for such a vibrationally induced charge flow. Most importantly, this also permits unambiguous identification of where the charge density is moving with respect to the molecular bonding framework.

The wavefunction results summarized in Fig. 9 reveal particularly clearly strong differential electron density effects for CH_2Cl and CH_2Br halomethyl radicals, with weaker "charge sloshing" contributions for CH_2F and CH_2I (not shown). For each of these species, there is visual evidence for an additional electron flow outward along the CX bond, adding constructively to the HCH transition dipole moment. Conversely, asymmetric CH_2 stretch excitation, although of course facilitating charge displacement along the b axis, cannot induce a charge flow parallel to the CX bond by symmetry. Indeed, the differential density plots indicate a modest counter flow of charge on the C atom that would even interfere destructively with the conventional bond-dipole transition moment for the asymmetric stretch. Simply summarized, the differential electron density plots in Fig. 9 provide clear theoretical support and a mechanism for preferential enhancement of symmetric over asymmetric CH_2 stretch intensities in the series of halomethyl radicals, as further confirmed by the data in Fig. 8.

V. SUMMARY AND CONCLUSION

First high-resolution infrared data in the CH stretching region for jet cooled CH_2I radicals have been presented. Sub-Doppler absorption spectra for excitation into the first symmetric (ν_2) vibrational band system have been obtained and analyzed within a rigid-rotor asymmetric top + spin rotation Hamiltonian framework. This analysis provides precise values for principal rotational constants (A, B, C), spin-rotation matrix elements (ε_{aa}, ε_{bb}, ε_{cc}), and band origin for the $v = 1$ symmetric CH_2 stretch manifold. We have also performed spectral searches over a wide frequency range (3143.8 cm^{-1} to 3212 cm^{-1}) for the corresponding asymmetric stretch band. This permits us to place an upper limit on the integrated I_{sym}/I_{asym} ratio of >25:1 which is in very poor agreement with bond-dipole model predictions of ≈1:3.

This provides clear support for substantial enhancement in the symmetric-stretch transition dipole moment by vibrationally induced displacement of local electron density in the total wavefunction, i.e., the so-called "charge-sloshing" mechanism, as highlighted previously by Whitney *et al.*[35] and McCoy and co-workers.[50] Additional evidence for the existence of this mechanism is obtained from the *ab initio* calculation of *differential* electron density wavefunction plots as a function of displacement along the symmetric and asymmetric CH_2 stretch normal mode coordinate. Notably, this analysis reveals a significant (A_1 symmetry) electron displacement outward along the CI bond axis with symmetric stretch excitation, which constructively adds to the dipole moment derivative and dramatically increases the infrared intensity. Conversely, vibrational excitation along the asymmetric stretch normal mode coordinate is of the wrong symmetry (B_2) to induce charge sloshing along the CI bond axis, thus yielding a transition dipole moment matrix element unenhanced (and even weakly diminished) by such a mechanism.

ACKNOWLEDGMENTS

This work has been supported by grants from the Department of Energy (Grant No. DE-FG02-09ER16021), with initial funds for construction of the slit-jet laser spectrometer provided by the National Science Foundation (Grant Nos. CHE 1266416 and PHY 1734006). We would also like to thank Dr. Stephen V. ONeil for many helpful discussions with respect to the most effective calculation, analysis, and visual representation of the electron difference density plots.

[1]A. Saiz-Lopez, J. M. C. Plane, A. R. Baker, L. J. Carpenter, R. von Glasow, J. C. G. Martin, G. McFiggans, and R. W. Saunders, Chem. Rev. **112**(3), 1773 (2012).
[2]E. S. Foreman and C. Murray, J. Phys. Chem. A **119**(34), 8981 (2015).
[3]J. G. Calvert and S. E. Lindberg, Atmos. Environ. **38**(30), 5087 (2004).
[4]*Handbook of Advanced Plasma Processing Techniques* (Springer Verlag, Berlin, 2000).
[5]R. E. Tapscott, R. S. Sheinson, V. Babushok, M. R. Nyden, and R. G. Gann, *NIST Technical Notes 1443* (NIST, 2001).
[6]J. Z. Su and A. K. Kim, Fire Technol. **38**(1), 7 (2002).
[7]M. E. Jacox and D. E. Milligan, J. Chem. Phys. **53**(7), 2688 (1970).
[8]D. W. Smith and L. Andrews, J. Chem. Phys. **55**(11), 5295 (1971).
[9]D. W. Smith and L. Andrews, J. Chem. Phys. **58**(12), 5222 (1973).
[10]L. C. Allen, J. Am. Chem. Soc. **111**(25), 9003 (1989).
[11]E. S. Whitney, D. Feng, and D. J. Nesbitt, J. Chem. Phys. **125**(5), 054304 (2006).
[12]P. Marshall, G. N. Srinivas, and M. Schwartz, J. Phys. Chem. A **109**(28), 6371 (2005).
[13]R. Criegee and G. Wenner, Justus Liebigs Ann. Chem. **564**(1), 9 (1949).
[14]C. A. Taatjes, G. Meloni, T. M. Selby, A. J. Trevitt, D. L. Osborn, C. J. Percival, and D. E. Shallcross, J. Am. Chem. Soc. **130**(36), 11883 (2008).
[15]O. Welz, J. D. Savee, D. L. Osborn, S. S. Vasu, C. J. Percival, D. E. Shallcross, and C. A. Taatjes, Science **335**(6065), 204 (2012).
[16]J. C. Mossinger, D. E. Shallcross, and R. A. Cox, J. Chem. Soc., Faraday Trans. **94**(10), 1391 (1998).
[17]G. Herzberg and J. Shoosmith, Can. J. Phys. **34**(5), 523 (1956).
[18]R. W. Fessenden and R. H. Schuler, J. Chem. Phys. **39**(9), 2147 (1963).
[19]W. L. S. Andrews and G. C. Pimentel, J. Chem. Phys. **44**(6), 2527 (1966).
[20]D. E. Milligan and M. E. Jacox, J. Chem. Phys. **47**(12), 5146 (1967).
[21]L. Andrews and G. C. Pimentel, J. Chem. Phys. **47**(9), 3637 (1967).
[22]A. Snelson, J. Phys. Chem. **74**(3), 537 (1970).
[23]M. E. Jacox, J. Mol. Spectrosc. **66**(2), 272 (1977).
[24]C. Yamada, E. Hirota, and K. Kawaguchi, J. Chem. Phys. **75**(11), 5256 (1981).
[25]S. Davis, D. T. Anderson, G. Duxbury, and D. J. Nesbitt, J. Chem. Phys. **107**(15), 5661 (1997).
[26]N. E. Triggs, M. Zahedi, J. W. Nibler, P. Debarber, and J. J. Valentini, J. Chem. Phys. **96**(3), 1822 (1992).
[27]L. Y. Tan, A. M. Winer, and G. C. Pimentel, J. Chem. Phys. **57**(9), 4028 (1972).
[28]T. Amano, P. F. Bernath, C. Yamada, Y. Endo, and E. Hirota, J. Chem. Phys. **77**(11), 5284 (1982).
[29]M. A. Roberts, C. Savage, F. Dong, E. N. Sharp-Williams, A. B. McCoy, and D. J. Nesbitt, J. Chem. Phys. **136**(23), 234308 (2012).
[30]R. W. Fessenden and R. H. Schuler, J. Chem. Phys. **43**(8), 2704 (1965).
[31]G. A. Carlson and G. C. Pimentel, J. Chem. Phys. **44**(10), 4053 (1966).
[32]D. E. Milligan and M. E. Jacox, J. Chem. Phys. **48**(5), 2265 (1968).
[33]Y. Endo, C. Yamada, S. Saito, and E. Hirota, J. Chem. Phys. **79**(4), 1605 (1983).
[34]S. Bailleux, P. Drèan, Z. Zelinger, and M. Godon, J. Mol. Spectrosc. **229**(1), 140 (2005).
[35]E. S. Whitney, T. Haeber, M. D. Schuder, A. C. Blair, and D. J. Nesbitt, J. Chem. Phys. **125**(5), 054303 (2006).
[36]H. Ozeki, T. Okabayashi, M. Tanimoto, S. Saito, and S. Bailleux, J. Chem. Phys. **127**(22), 224301 (2007).
[37]S. Bailleux, P. Drèan, Z. Zelinger, S. Civis, H. Ozeki, and S. Saito, J. Chem. Phys. **122**(13), 134302 (2005).
[38]S. Bailleux, P. Kania, J. Skrinsky, T. Okabayashi, M. Tanimoto, S. Matsumoto, and H. Ozeki, J. Phys. Chem. A **114**(14), 4776 (2010).
[39]M. J. Frisch, G. W. Trucks, H. B. Schlegel, G. E. Scuseria, M. A. Robb, J. R. Cheeseman, J. J. A. Montgomery, T. Vreven, K. N. Kudin, J. C. Burant, J. M. Millam, S. S. Iyengar, J. Tomasi, V. Barone, B. Mennucci, M. Cossi, G. Scalmani, N. Rega, G. A. Petersson, H. Nakatsuji, M. Hada, M. Ehara, K. Toyota, R. Fukuda, J. Hasegawa, M. Ishida, T. Nakajima, Y. Honda, O. Kitao, H. Nakai, M. Klene, X. Li, J. E. Knox, H. P. Hratchian, J. B. Cross, C. Adamo, J. Jaramillo, R. Gomperts, R. E. Stratmann, O. Yazyev, A. J. Austin, R. Cammi, C. Pomelli, J. W. Ochterski, P. Y. Ayala, K. Morokuma, G. A. Voth, P. Salvador, J. J. Dannenberg, V. G. Zakrzewski, S. Dapprich, A. D. Daniels, M. C. Strain, O. Farkas, D. K. Malick, A. D. Rabuck, K. Raghavachari, J. B. Foresman, J. V. Ortiz, Q. Cui, A. G. Baboul, S. Clifford, J. Cioslowski, B. B. Stefanov, G. Liu, A. Liashenko, P. Piskorz, I. Komaromi, R. L. Martin, D. J. Fox, T. Keith, M. A. Al-Laham, C. Y. Peng, A. Nanayakkara, M. Challacombe, P. M. W. Gill, B. Johnson, W. Chen, M. W. Wong, C. Gonzalez, and J. A. Pople, GAUSSIAN 09, Revision B.01 (Gaussian, Inc., Pittsburgh, PA, 2003, 2016).
[40]S. Davis, M. Farnik, D. Uy, and D. J. Nesbitt, Chem. Phys. Lett. **344**(1-2), 23 (2001).
[41]D. Herriott, R. Kompfner, and H. Kogelnik, Appl. Opt. **3**(4), 523 (1964).
[42]A. S. Pine, J. Opt. Soc. Am. **64**(12), 1683 (1974).
[43]L. H. Deng, X. M. Gao, Z. S. Cao, W. D. Chen, Y. Q. Yuan, W. J. Zhang, and Z. B. Gong, Opt. Commun. **268**(1), 110 (2006).
[44]E. Riedle, S. H. Ashworth, J. T. Farrell, and D. J. Nesbitt, Rev. Sci. Instrum. **65**(1), 42 (1994).
[45]A. S. Pine, J. Opt. Soc. Am. **66**(2), 97 (1976).
[46]L. S. C. Martins, F. A. L. de Souza, G. A. Ceolin, F. E. Jorge, R. C. de Berredo, and C. T. Campos, Comput. Theor. Chem. **1013**, 62 (2013).
[47]F. Dong, S. Davis, and D. J. Nesbitt, J. Phys. Chem. A **110**(9), 3059 (2006).
[48]C. M. Western, PGOPHER version 10.0, University of Bristol Research Data Repository, 2017.
[49]C. M. Western, J. Quant. Spectrosc. Radiat. Transfer **186**, 221 (2017).
[50]A. B. McCoy, J. Phys. Chem. B **118**(28), 8286 (2014).
[51]E. Hirota, *High-Resolution Spectroscopy of Transient Molecules* (Springer Verlag, Berlin, 1985).
[52]J. K. G. Watson, in "Vibrational spectra and structure," edited by J. Durig (Elsevier, Amsterdam, 1977), Vol. 6, p. 1.
[53]S. C. Wang, Phys. Rev. **34**(2), 243 (1929).
[54]J. R. Donaldson and T. V. Tryon, "User's guide to STARPAC," NIST internal report, 86-3448 (1990).
[55]S. Horvath, A. B. McCoy, B. M. Elliott, G. H. Weddle, J. R. Roscioli, and M. A. Johnson, J. Phys. Chem. A **114**(3), 1556 (2010).
[56]A. B. McCoy, T. L. Guasco, C. M. Leavitt, S. G. Olesen, and M. A. Johnson, Phys. Chem. Chem. Phys. **14**(20), 7205 (2012).
[57]J. R. Roscioli, E. G. Diken, M. A. Johnson, S. Horvath, and A. B. McCoy, J. Phys. Chem. A **110**(15), 4943 (2006).